Proceedings of the ASME 2014 International Gas Turbine Institute
ASME/IGTI 2014
June 16-20, 2014, Düsseldorf, Germany

GT2014-25307

ON PREDICTING THE PHENOMENON OF SURFACE FLOW CONVERGENCE IN WIND FARMS

Suganthi Selvaraj*

Department of Aerospace Engineering,
Iowa State University,
Ames, IA, 50011,
518-294-1200,
suganthi@iastate.edu

Anupam Sharma †

Department of Aerospace Engineering,
Iowa State University,
Ames, Iowa, 5011, U.S.A.
(515) 294 2884,
sharma@iastate.edu

ABSTRACT

A systematic analysis of a single-rotor horizontal axis wind turbine aerodynamics is performed to obtain a realistic potential maximum efficiency. It is noted that by including the effects of swirl, viscosity and finite number of blades, the maximum aerodynamic efficiency of a HAWT is within a few percentage points of the efficiency of commercially-available turbines. The need for investigating windfarm (as a unit) aerodynamics is thus highlighted.

An actuator disk model is developed and implemented in the OpenFOAM software suite. The model is validated against 1-D momentum theory, blade element momentum theory, as well as against experimental data. The validated actuator disk model is then used to investigate an interesting microscale meteorological phenomenon called "flow convergence" caused by an array of wind turbines. This phenomenon is believed to be caused by the drop of pressure in wind farms. Wind farm numerical simulations are conducted with various approximations to investigate and explain the flow convergence phenomenon.

Nomenclature

a	axial induction = $1 - U_d/U_\infty$
a'	angular induction = $U_\theta/(2\Omega r)$
A_d	Area of the actuator disk
c_d	sectional drag coefficient
c_l	sectional lift coefficient
c_N	thrust force coefficient
C_P	non-dimensional power coefficient
C_T	non-dimensional thrust coefficient
c_τ	torque force coefficient
l	any length
r_{tip}	tip radius
U	axial velocity
u	any velocity
u^*	friction velocity
U_{rel}	relative flow velocity magnitude
z_0	surface roughness length
z_g	Location of the ground
κ	Karman's constant
λ	blade speed to flow speed ratio; inverse of advance ratio
Ω	angular rotation speed of the rotor/disk
τ	aerodynamic torque
ξ	radius non-dimensionalized by tip radius
$[\,]_d$	condition at actuator disk (rotor plane of rotation)
$[\,]_r$	at radial location r
$[\,]_w$	condition at Trefftz plane (far downstream of the rotor)

*Graduate Student
†Assistant Professor.

INTRODUCTION

The Betz-Lancaster-Zhukowski limit of aerodynamic power coefficient, $C_P = 16/27$ is often casually referred to as the highest obtainable efficiency of a single-rotor horizontal axis wind turbine (HAWT). The realizable, practical limit of a torque-based, finite-bladed HAWT, operating in a viscous fluid is actually much (of the order 10%) lower. A more "practical" limit on C_P for a single-rotor HAWT is thus proposed. After accounting for these (almost unavoidable) physical limits, this "practical" limit on C_P is found to be just a few percentage points higher than that of modern, utility-scale HAWTs. In contrast, array losses due to wake interference between turbines can lead to aerodynamic losses anywhere between 8-40% [1]. These losses are caused by the ingestion of velocity defect (wake) of upstream turbines by downstream turbines. Turbulent mixing between the wake stream and the freestream re-energizes the flow and reduces the wake deficit. The relevant length scale for this turbulent mixing is the turbine diameter. From the perspective of windfarm efficiency, modeling of individual blade boundary layer is therefore not required (as long as its effect on the same turbine is accounted for). An even simpler approach, to completely ignore the rotor blades and model their effect by an actuator disk is adopted. Body forces, equivalent of the thrust and torque forces experienced by the HAWT, are applied at the actuator disk. These are simulated by adding a source term (body force) to the momentum equation. The strength of the source term is computed using 2-D airfoil theory. For this paper, the *SimpleFOAM* solver of the OpenFOAM solver suite is employed. SimpleFOAM solves the incompressible, Reynolds Averaged Navier Stokes (RANS) equations. The $k-\varepsilon$ turbulence closure model is used.

This model is implemented in OpenFOAM to study single-turbine and wind farm aerodynamics. The OpenFOAM model is first validated by comparing against (a) analytical results from the 1-D momentum theory for HAWTs, and (2) experimental data and results from the blade element momentum (BEM) theory for a HAWT. The model is then used to investigate an interesting phenomenon observed in wind turbine arrays called "flow convergence". Flow coming at an angle to a turbine array has been observed in experiments [2] to align itself to the direction of the array. This observation is supported by the OpenFOAM calculations described in this report. It is hypothesized that the reason for this flow convergence is due to a microscale pressure gradient that is setup due to turbine arrays. Numerical results using the actuator disk model support this hypothesis. While the analysis is simplistic, in that is uses RANS equations, it is able to predict the phenomenon and also provide some substance to the hypothesis for its cause.

The remainder of the paper is arranged as follows. A systematic entitlement study of aerodynamic performance of a HAWT is first presented. The OpenFOAM actuator disk model is then described with details on source modeling. This is followed by a detailed validation of the model against 1-D momentum theory for a uniformly-loaded rotor, and against experiments and BEM theory for two HAWTs in uniform flow. A hypothetical windfarm is then constructed with periodic boundary conditions in (almost) cross-flow direction to represent an infinite array of turbines. Several simulations with varying assumptions are then performed to investigate the phenomenon of flow convergence. The final section presents some conclusions from the study.

MAXIMUM POTENTIAL C_P FOR A HAWT OPERATING IN ISOLATION IN UNIFORM FLOW

Several theories with varying degrees of approximations are available to analyze aerodynamic efficiency of a horizontal axis wind turbine (HAWT). The simplifications in these theories typically neglect one or more physical phenomena that reduce the practically attainable efficiency. The simplest of these theories, for example, is the 1-D actuator disk theory that gives the Betz limit [3] for aerodynamic efficiency of a HAWT of $C_P = 16/27 (\sim 0.593)$. Figure 1 shows a schematic of the actuator disk model.

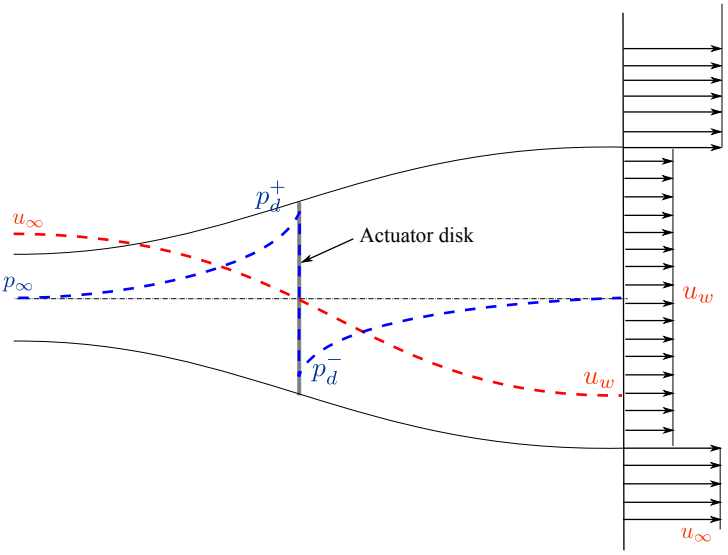

FIGURE 1: A schematic of 1-D momentum theory model for a HAWT.

1-D Momentum Theory

The 1-D momentum theory makes the simplifying assumptions that the flow is (1) one-dimensional (zero swirl), and (2) inviscid. Mass conservation, momentum balance, and energy

conservation can be expressed as

$$\begin{aligned}
\rho U_\infty A_\infty &= \rho A_d U_d = \rho U_w A_w, \text{ (mass)} \\
\rho U_d A_d (U_\infty - U_w) &= (p_d^+ - p_d^-) A_d, \text{ (momentum)} \\
p_d^+ + \frac{1}{2}\rho {U_d}^2 &= p_\infty + \frac{1}{2}\rho {U_\infty}^2, \text{or} \\
p_d^- + \frac{1}{2}\rho {U_d}^2 &= p_\infty + \frac{1}{2}\rho {U_w}^2 \text{ (energy)}
\end{aligned} \tag{1}$$

Representing the induced velocity at the actuator disk as a fraction, a of the freestream velocity, U_∞ as $-a\ U_\infty$, Eqs. 1 can be manipulated to write the thrust (axial force) force coefficient, C_T and power coefficient, C_P in the form

$$\begin{aligned}
C_T &= \mathrm{T}/(1/2\rho {U_\infty}^2 A_d) = 4a(1-a), \text{and} \\
C_P &= \mathrm{P}/(1/2\rho {U_\infty}^3 A_d) = 4a(1-a)^2.
\end{aligned} \tag{2}$$

HAWTs are designed to maximize C_P, while propellers maximize C_T. The extrema for $C_P(a)$ are obtained by solving $\mathrm{d}C_P/\mathrm{d}a = 0$, which gives the maximum $C_P = 16/27$ at $a = 1/3$. This maximum C_P (limit) is also known as the *Betz* limit, or more appropriately the Betz-Lancaster-Zhukowski limit. Figure 2 plots the variation of C_P and C_T with axial induction factor, a given by the 1-D momentum theory.

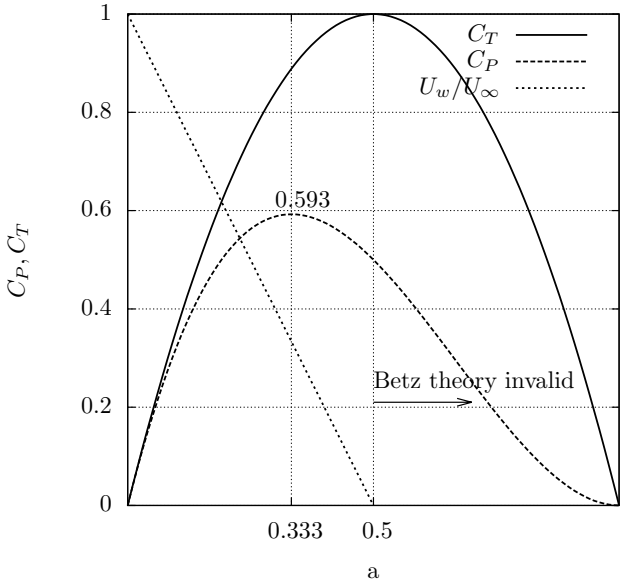

FIGURE 2: C_P and C_T values as functions of induction, a from the 1-D momentum theory.

Actuator Disk With Swirl

The 1-D momentum theory ignores the fact that HAWTs are torque devices. Torque generation requires a change in the angular momentum of the fluid. This is incorporated by allowing the flow to swirl behind the actuator disk. The swirl velocity, U_θ behind the disk is non-dimensionalized to get tangential induction factor, $a' = U_\theta/(2\Omega r)$. To satisfy radial equilibrium (force balance in radial direction), a, a' and other quantities have to vary radially and the flow has to be analyzed in 2-D (axial and radial); azimuthal symmetry is still assumed. This is typically done by discretizing the actuator disk into multiple annular sections. Conserving angular momentum at each annular strip of width δr at radius r (area, $\delta A_d = 2\pi r \delta r$) gives:

$$\begin{aligned}
\delta\tau &= r\,\rho\,\delta A_d\,U_\infty(1-a)U_\theta, \\
\delta P &= \delta\tau\,\Omega = \left[\frac{1}{2}\rho\,\delta A_d U_\infty^3\right]\,4{\lambda_r}^2 a'(1-a), \text{ and} \\
C_{P\mathrm{sec}} &= 4{\lambda_r}^2 a'(1-a).
\end{aligned} \tag{3}$$

In above, λ_r denotes the ratio $\Omega r/U_\infty$, which at $r = R_{\mathrm{TIP}}$ is the blade tip speed ratio (TSR), λ and $C_{P\mathrm{sec}}$ is the sectional non-dimensional power coefficient. The overall C_P is obtained as area-weighted average of $C_{P\mathrm{sec}}$.

$$C_P = \frac{1}{\pi R_{\mathrm{TIP}}^2}\int_0^{R_{TIP}} C_{P\mathrm{sec}}\,2\pi r\,\mathrm{d}r = 8\lambda^2\int_0^1 \xi^3 a'(1-a)\mathrm{d}\xi, \tag{4}$$

where $\xi = r/R_{\mathrm{TIP}}$ is the non-dimensional radius. Maximum C_P relation can again be obtained and distributions of a and a' with radius computed analytically. Figure 3 shows the variation of induced velocity fractions, a, a' with λ_r ($\lambda_r = \xi\lambda$ represents variation with radius for a fixed λ) and the variation of $C_{P\max}$ with λ. Modern, utility-scale HAWTs have design tip speed ratios between $6-14$. Figure 3 suggests that wake rotation losses can be safely ignored in a HAWT with a high λ.

Effect of Finite Number of Blades

While modeling of a HAWT rotor using an actuator disk provides elegant, relatively simple analytical expressions for computing C_P, it discounts the fact that real turbines have finite number of blades. This finiteness leads to circumferential variation of induction factors (a, a' are now functions of r and θ), and this circumferential non-uniformity generates additional losses.

In momentum-theory based approaches, the effect of finite number of blades can be approximately accounted for by hub/tip loss "corrections". These corrections are specified as factors that are multiplied with aerodynamic forces. These factors mimic the lift reduction due to induction from trailing vorticity in a finite-span blade. Prandtl's tip/hub loss model e.g., is widely used in

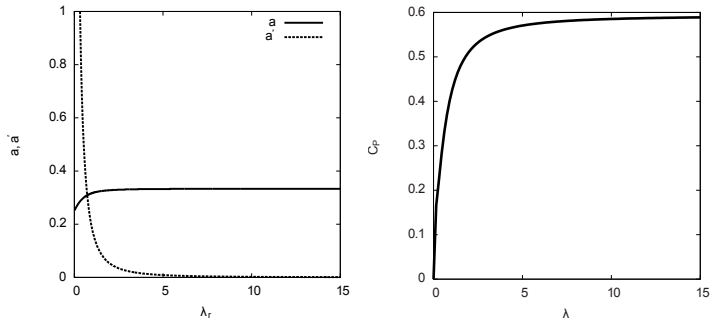

(a) a, a' as functions of λ_r (b) $C_{P\max}$

FIGURE 3: Variation of (a) axial & swirl induction with λ_r, and (b) maximum C_P as a function of λ.

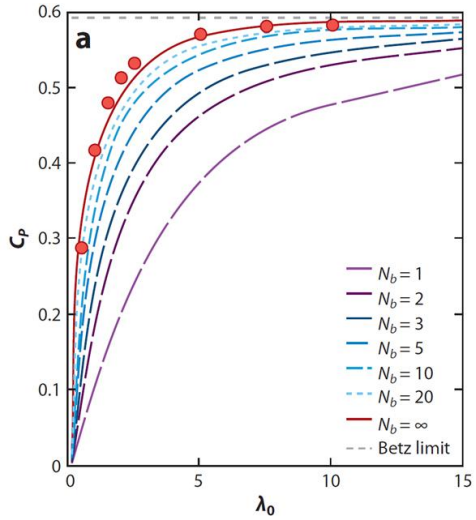

FIGURE 4: C_P versus λ curves for varying number of blades of a HAWT. Points represent generalized momentum theory solutions and lines are from the theory presented by Okulov [5]. Borrowed from Okulov and Sørensen [6].

HAWT aerodynamic analysis. In contrast, in models based on vortex theory, each blade is represented by a line (or plane/array) of bound vortices and the wake by a helical vortex sheet extending from the trailing edge of each blade to far enough downstream (Trefftz plane). Induction is computed using the Biot-Savart's law and aerodynamic forces on blades are computed using the Kutta-Jukowski theorem.

Ideal efficiency for a finite-bladed HAWT has been computed by Goldstein [4] (his analysis was limited to number of blades = 2 and 4), and more recently by Okulov and Sorensen in a series of papers [5–7]. Okulov [5] proposed a closed form solution for the velocity field induced by each filament of the circulation distribution in the wake. Using that analytical solution, the Goldstein circulation function and hence the power coefficient of an ideal turbine with arbitrary number of blades are determined. Their final result of the variation of the aerodynamic power coefficient C_P with the number of blades of a HAWT is replicated in Fig. 4. The aerodynamic benefit of using more blades is evident in Fig. 4. This benefit however reduces as the tip speed ratio is increased. Also, the effect of viscous drag is ignored in this analysis, which again shifts the C_P benefit in favor of less number of blades.

Effect of Viscosity

In the blade element momentum (BEM) theory, the rotor is represented by a series of radial strips, which essentially operate independent of each other. In each radial strip, the thrust and torque from the momentum theory are equated to those from the blade element (airfoil strip) theory. Using the BEM theory, Wilson *et al.* [8] provides a simple equation (Eq. 5) for ideal C_P while accounting for profile drag and tip induction losses. According to Wilson *et al.* [8], the fit of this equation to data is within 0.5% for tip speed ratios between 4 and 20, for drag to lift ratios between 0 and 0.04, and for number of blades from 1 to 3.

$$C_{P\max} = \frac{16}{27}\lambda\left[\frac{N_b^{2/3}}{1.48+\left(N_b^{2/3}-0.04\right)\lambda+0.0025\lambda^2} - \frac{C_d}{C_l}\frac{1.92N_b\lambda}{1+2\lambda N_b}\right]. \quad (5)$$

Equation 5 is used to evaluate the impact of viscosity (modeled by changing C_l/C_d) on C_P. A nominal value of area-averaged, $C_l/C_d = 100$ is used to generate the "blue" curve in Fig. 5. The maximum of this curves has $C_P \sim 0.5$, which is within a few percentage points of the C_P of modern HAWTs especially when they are in "mint" condition (surface is smooth and clean of bugs/debris).

Thus while there is always merit in improving the aerodynamic performance of a single turbine, it appears that the return on investment is getting lower and lower. In contrast, the potential benefit of improving wind farm (as a unit) performance appear to be much larger based on experimental evidence. This study is on analyzing wind farm aerodynamics however the focus is not on predicting or improving farm efficiency, rather on explaining an interesting microscale meteorological phenomenon caused by wind farms.

ACTUATOR DISK MODEL IN OPENFOAM

The OpenFOAM software suite is chosen for the present investigation. OpenFOAM is essentially a group of C++ libraries used to create solvers. Some commonly used numerical solvers for fluid flow simulations are provided in the software pack-

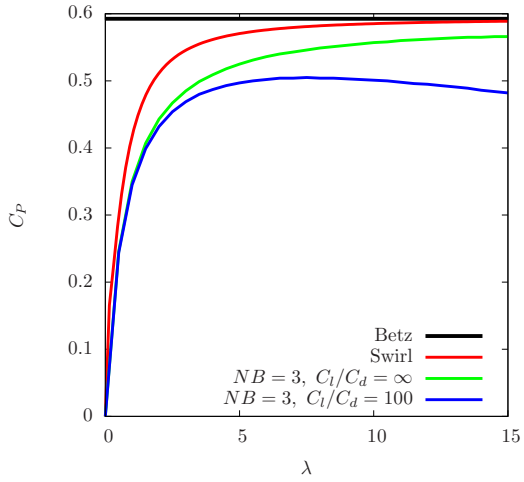

FIGURE 5: Maximum possible C_P with various approximations.

age. The particular solver (with some additions and modification) used in the present study is called *SimpleFOAM*. The governing equations solved by the SimpleFOAM solver are the incompressible RANS equations:

$$\frac{\partial \bar{u}_i}{\partial x_i} = 0, \text{ and,} \tag{6}$$

$$\bar{u}_j \frac{\partial \bar{u}_i}{\partial x_j} = -\frac{1}{\rho}\frac{\partial \bar{p}}{\partial x_i} - \nu \frac{\partial^2 \bar{u}_i}{\partial {x_j}^2} - \frac{\partial \overline{u_i' u_j'}}{\partial x_j} + \frac{f_i}{\rho}. \tag{7}$$

The Reynolds stress tensor, $\overline{u_i' u_j'}$ is modeled using eddy ("turbulent") viscosity as $\nu_t \frac{\partial \overline{u_i}}{\partial x_j}$. Turbulent viscosity, ν_t is obtained using turbulent kinetic energy, k and dissipation, ε, which are themselves obtained by solving a transport equation for each. The term f_i represents body force per unit volume. A finite volume in the computational domain is defined (corresponding to rotor swept area times small thickness) where body forces are applied to model the effect of the rotor. The magnitude of the body force and its direction are obtained using the 2-D airfoil theory. By probing the CFD at the rotor disk, the local velocity is obtained. Using the prescribed blade pitch and twist, ϕ, the local angle of attack, α to the airfoil is obtained. Two-dimensional airfoil polars ($c_l - \alpha$ and $c_d - \alpha$ curves) combined with local velocity and airfoil chord give the sectional lift, dL and drag, dD (see Fig. 6). Components of these forces (summed over all turbine blades) along the coordinate axes are then used as body forces in the corresponding momentum equations. These forces are distributed over a volume and a Gaussian distribution is applied along the flow direction following Mikkelsen [9]. The actuator disk model has been implemented in OpenFOAM and some validation results are presented next.

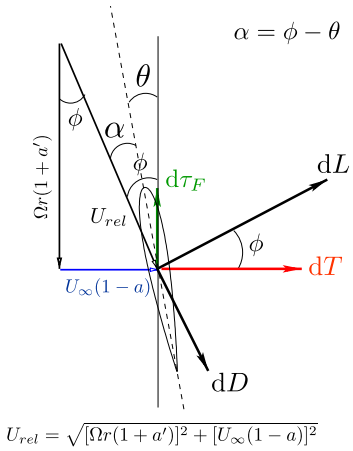

FIGURE 6: Flow vectors and aerodynamic forces on an airfoil.

Validation

1-D Momentum Theory The actuator disk CFD model is first validated against the 1-D momentum theory for a HAWT in uniform flow. The actuator disk in this case represents the uniformly-loaded rotor. The thrust force (as calculated using Eq. 2) is applied to simulate the effect of the rotor. Due to axi-symmetry in the problem, only a small sector (2-D) of the rotor disk needs to be modeled. A general setup using non-dimensional variables is used. The following non-dimensionalization

$$\tilde{l} = l/r_{tip} \text{ and}$$
$$\tilde{u} = u/U_\infty,$$

makes the tip radius unity, freestream velocity equal to 1, and the tip speed of the rotor equal to the tip speed ratio, λ. The mesh is heavily clustered where the body force source terms are applied as well as in the slipstream where flow gradients are expected. Figure 7 shows the grid and solutions for a uniformly-loaded rotor for two different loading conditions. Disk loading is governed by C_T (Eq. 2). Larger streamtube expansion can be seen in the case of the more heavily loaded disk. Figure 8 shows comparisons of C_T and C_P against Eq. 2 for various values of axial induction a. Figure 8 plots calculated a, C_T and C_P against specified axial induction, a. As the specified induction approaches 0.5 (the limit where 1-D momentum theory breaks down), the computed induction factor does not quit follow. Therefore, the results are plotted in Fig. 8 (b) against computed axial induction factor. Good agreement between data and theory is observed for low-loading conditions. Larger differences at higher loading conditions are expected as the flow does not remain one dimensional.

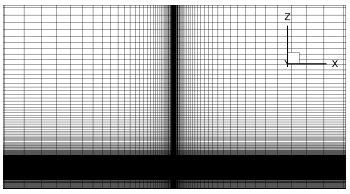

(a) Grid

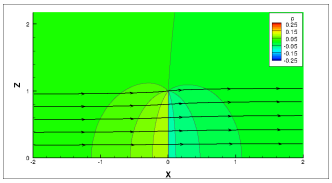

(b) $a = 0.1$

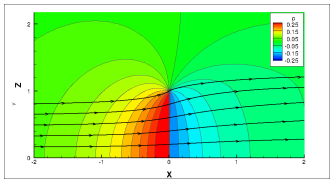

(c) $a = 0.5$

FIGURE 7: Two-dimensional grid and simulations of the uniformly loaded rotor.

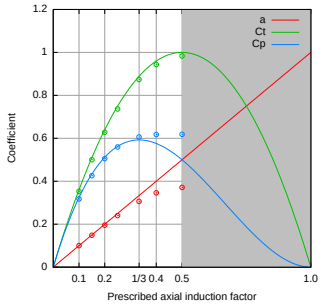

(a) Specified induction

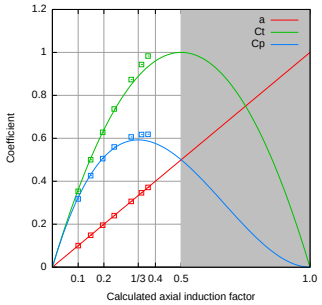

(b) Computed induction

FIGURE 8: Validation against analytical results using 1D momentum theory for C_T and C_P. Symbols represent numerically computed values; lines represent color-matched analytical solutions. Plot on the right uses the computed value of 'a' on the abscissa.

Validation against Turbine Data The actuator disk model is next compared against experimental data as well as solutions obtained using the blade element momentum (BEM) theory for two turbines: (1) the Risϕ turbine [10], and (2) the NREL phase VI turbine [11].

Risϕ Turbine The Risϕ turbine is a stall-controlled turbine that has a 3-bladed rotor with a diameter of 19 m. The turbine can operate at two rotational speeds, 35.6 and 47.5 RPM which correspond to maximum powers of 32 kW and 95 kW respectively. The twist and chord distributions along the radius of the blade are shown in Fig. 9 (a). The blades were designed using the NACA 63n-2nn series airfoils. The c_l and c_d distributions for these airfoils were obtained from Abbott and Doenhoff [12] and have been corrected for the actual Reynolds number for the test blade.

Figure 9 (b) compares the overall performance of the Risϕ turbine over a range of tip speed ratios, λ. Since the rotor RPM is fixed, increasing tip speed ratio is equivalent to reduction in flow speed. The comparison between data, BEM theory and actuator disk results is good near peak performance (where C_P is maximum). As the tip speed ratio reduces, the angle-of-attack experience by the blade increases and for small enough λ, parts of the blade stall. The BEM theory as well as actuator disk results use 2-D airfoil polars. It is known that the 3-dimensionality of the blade alleviates airfoil stall and permits operation of the blade at higher angle of attack. This is the reason why the data shows a higher value of C_P at small λ. As λ is increased past the peak C_P value, the thrust coefficient, C_T of the turbine continues to increase. The thrust coefficient, C_T increases beyond 1 right around $\lambda = 8$ in the actuator disk simulations. It is known that the flow behind a turbine is in the turbulent wake state for $C_T > 1$. The steady flow approximation does not hold anymore and this modeling approximation is believed to be responsible for the difference between modeling results and measured C_P. Note that the actuator disk results agree more with the BEM theory because of somewhat similar approximations made in the two approaches.

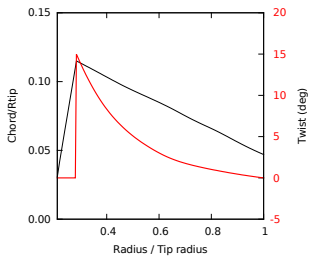

(a) Chord, twist

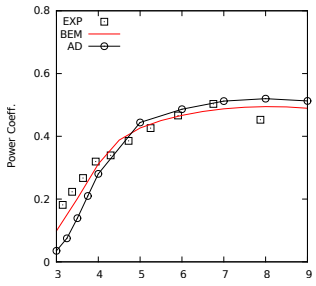

(b) $C_P - \lambda$ curve

FIGURE 9: The Risϕ rotor: (a) geometric chord and twist, and (b) $Cp - \lambda$ comparison between various measured data, BEM theory and actuator disk simulation results.

Figure 10 plots pressure contours and streamlines passing through the rotor disk for two tip speed ratios. The bottom 20% span of the blade does not produce significant aerodynamic forces; it is typically designed for structural integrity of the blade. The pressure contours reflect this design intent and insignificant pressure jump is observed across the rotor disk in the bottom 20% of the blade. The rotor is lightly loaded at $\lambda = 4.0$ compared to at $\lambda = 7.0$ as can be inferred from the $C_P - \lambda$ curve in Fig. 9 (b). The effect of loading can be seen in the pressure contours as

well as the streamtube expansion. The streamtube expands much more for the $\lambda = 7.0$ case.

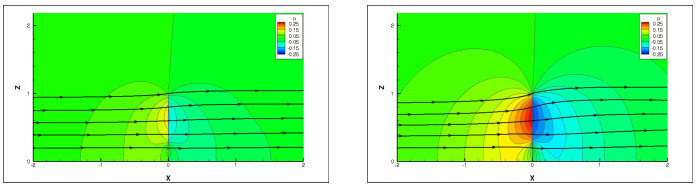

(a) $\lambda = 4.0$ (b) $\lambda = 7.0$

FIGURE 10: Pressure contours and streamlines through the Risoe Turbine (actuator disk simulation results) for two tip speed ratios.

Radial variations of the rotor torque force coefficient, C_τ and the thrust force coefficient, C_N are plotted in Fig. 11 (b) and (c) at $\lambda = 7$. These are defined as follows (see Fig. 6):

$$c_\tau = \mathrm{d}\tau_F \Big/ \left(\frac{1}{2}\rho_\infty U_{rel}^2 c\right) = c_l \sin(\phi) - c_d \cos(\phi), \text{ and}$$
$$c_N = \mathrm{d}T \Big/ \left(\frac{1}{2}\rho_\infty U_{rel}^2 c\right) = c_l \cos(\phi) + c_d \sin(\phi),$$

where, $\mathrm{d}\tau_F$ is the sectional force component in the plane of rotation of the rotor that contributes to the torque about the rotor axis, and $\mathrm{d}T$ is the sectional force component that contributes to the thrust loading on the turbine. In Fig. 11, the numerical results from actuator disk theory implementation in OpenFOAM are compared with results using the BEM theory. The torque force coefficient comparison is excellent. Larger differences near the tip region are observed for thrust force coefficient. There are two reasons for this: (1) the actuator disk model accounts for the radial flow near the tip. As the streamtube expands, the axial component of the velocity drops and that leads to reduction in angle of attack near the tip and hence the aerodynamic lift and drag, and (2) due to the differences in application of Prandtl's tip loss correction factor between the BEM theory and the actuator disk model. In the actuator disk model used here, the Prandtl's tip loss correction factor ($F < 1$) is multiplied to the lift force and the drag force is left un-corrected.

NREL Phase VI Rotor The NREL phase VI turbine has a two-bladed rotor which was designed with a single airfoil, NREL's S809, throughout the blade span (except near the root where a cylinder is used). The chord (non-dimensionalized by tip radius) and the blade twist distributions are shown in Fig. 12 (a). Figure 12 (b) compares the $C_P - \lambda$ curves obtained using the BEM theory and using the actuator disk model implementation in OpenFOAM. Good agreement is observed at high λ, while

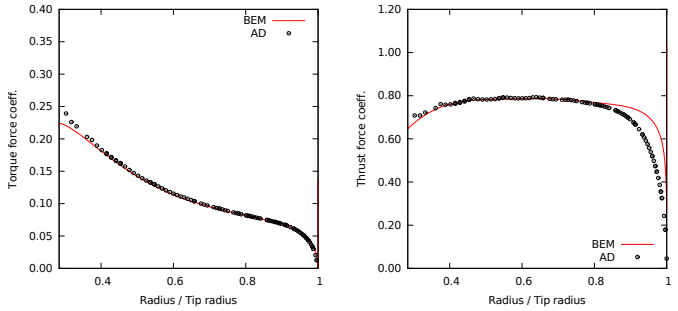

(a) c_τ (b) c_N

FIGURE 11: Torque force coefficient, c_τ and thrust force coefficient, c_N distributions compared between Actuator disk model predictions against BEM prediction.

relatively large differences between the actuator disk model and the BEM results are observed at small λ, similar to the observation for the Risϕ rotor. Figure 13 shows the pressure contours and streamlines for two values of λ.

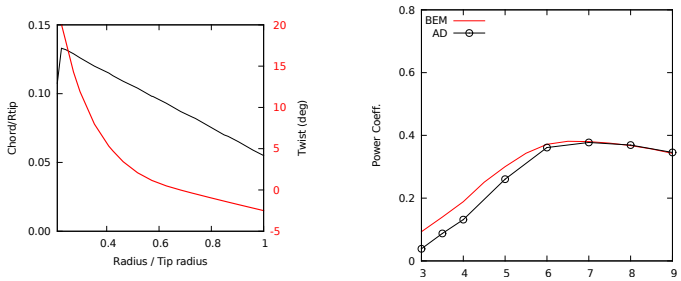

(a) Chord & twist (b) $C_P - \lambda$ curve

FIGURE 12: NREL phase VI rotor: (a) Chord and twist distribution, and (b) $C_P - \lambda$ curve.

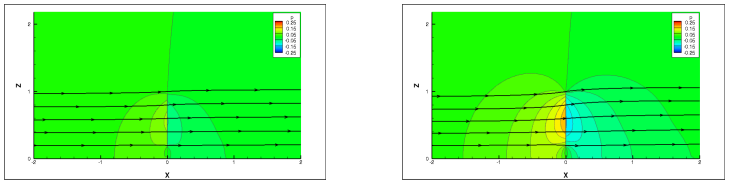

(a) $\lambda = 4.0$ (b) $\lambda = 7.0$

FIGURE 13: Pressure contours and streamlines through the NREL-VI Turbine (actuator disk simulation results) for two tip speed ratios.

Profile comparisons between BEM and actuator disk solutions are carried out for $\lambda = 7.0$ (near peak turbine performance) and c_τ and c_N profiles are shown in Fig. 14. The agreement between the actuator disk theory results and BEM results is good for C_τ; larger differences are observed of c_N near the tip, consistent with the observations for the Risϕ rotor.

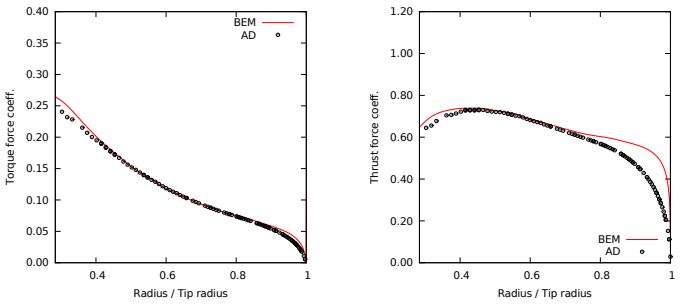

(a) c_τ (b) c_N

FIGURE 14: Torque force coefficient, c_τ and thrust force coefficient, c_N distributions compared between Actuator disk model predictions against BEM results.

SURFACE FLOW CONVERGENCE PHENOMENON

Recent experiments involving wind farm aerodynamic measurements have observed [2] an interesting atmospheric micro-scale phenomenon that is referred to as "flow convergence". It has been observed that a row of turbines aligns the flow, coming at an angle, with the direction of the turbine array (see illustration in Fig. 15). Figure 16 shows one set of experimental observations from a wind farm taken during neutral atmospheric stability condition. It shows the flow angle deviation (from incoming flow angle) observed close to the ground behind a few turbines in a wind farm. Similar measurements have also been made under stable and unstable atmospheric conditions and the flow convergence has been observed to be strongest during stable and weakest during unstable conditions. To authors' knowledge, there are no documented observations or explanations of this phenomenon in wind farms.

A plausible explanation for the surface flow convergence phenomenon is hypothesized here. As shown in Fig. 1, there is a sharp pressure drop across an isolated turbine rotor and then the pressure subsequently recovers to its free-stream value far downstream. In an array of turbines, this pressure recovery may not completely occur before the next downstream turbine further drops the pressure. In a large array of turbines therefore, the static pressure continues to drop through the turbine array. This drop in pressure creates a pressure gradient which acts along

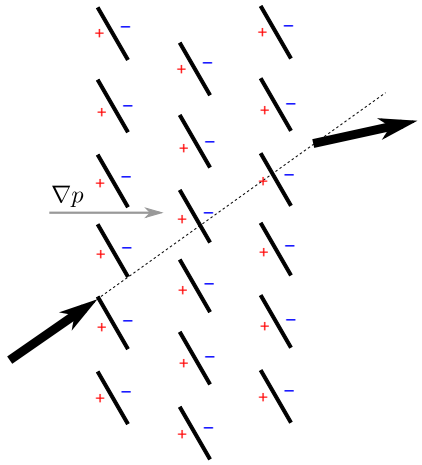

FIGURE 15: A schematic illustrating the micro-scale pressure gradient that gets set up in windfarms due to resistive forces from turbines.

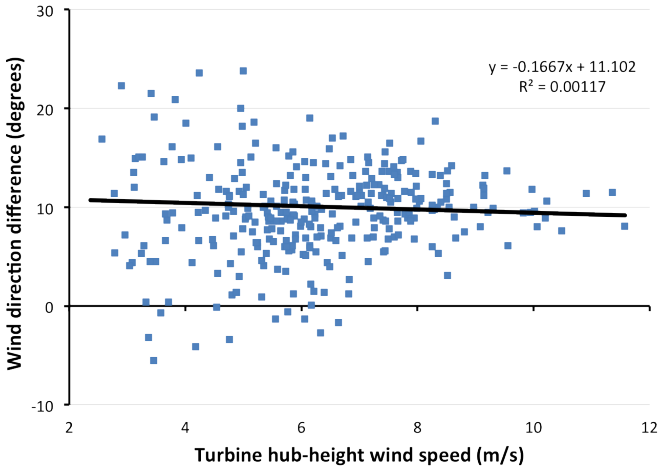

FIGURE 16: Experimental data showing surface flow convergence under neutral atmospheric stability conditions. Courtesy Takle [2].

the direction of the turbine array (high upstream and low downstream) as shown schematically in Fig. 15. Fluid is driven in the direction of this pressure gradient, aligning the flow with the turbine array. Wind turbine arrays thus affect the micro-scale meteorology.

To substantiate the hypothesis (to explain the flow convergence phenomenon) presented above, a few OpenFOAM simulations with the actuator disk model described earlier are performed. A hypothetical farm is simulated with inflow and outflow boundaries along the turbine row direction and periodic boundary conditions in the cross direction. Periodic boundary

conditions are chosen to simplify the problem by getting rid of the parameter of number of turbines in a row. Figure 17 shows a partial cross-section (as viewed from the top) of the domain listing the conditions applied at the boundaries. Zero-gradient condition is imposed on the velocity vector at the top boundary. The ground boundary is simulated as a slip wall (for inviscid simulations) as well as no-slip wall (for viscous simulations). The velocity profile at the inflow boundary is set to be either uniform (inviscid) or a logarithmic profile.

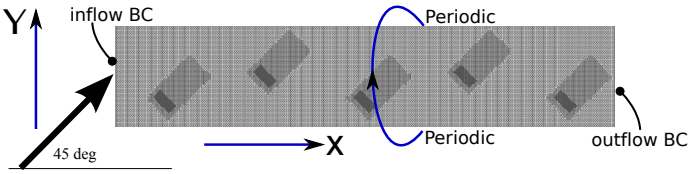

FIGURE 17: Simulation setup and mesh at turbine hub height. Partial domain with only five turbines shown for clarity

For our first analysis, we consider the ideal the problem of inviscid, uniform flow.

Inviscid Approximation

The flow is setup to come in at 45^0 to the turbine row. Figure 18 shows pressure contours on two planes: (1) at hub height, and (2) on the ground. Sharp pressure drops across each turbine (actuator disk) are clearly visible in the figure at hub height. There also exists an overall pressure drop along the turbine row, which is visible more clearly in the contour plot drawn on the ground. The flow is from left to right in the figure. Figure 19 draws contours of the local flow angle (w.r.t. x direction) at hub height and on the ground. At the inlet, the flow is uniform and at 45^0 to the turbine row. At the exit the flow angle is about 2-3 degrees smaller (more aligned with the turbine row direction). While this does not quantitatively agree with the experimental measurements, it is qualitatively in the right direction. The experimental data, which was measured near the ground, shows a deviation of around 10 degrees on average under neutral atmospheric stability conditions (see Fig. 16). The large difference between data and numerical results here is due to the inviscid flow (absence of planetary boundary layer) assumption used here; this will be proven in the next section as that assumption in the flow is relaxed.

Effect of Planetary Boundary Layer

The planetary boundary layer is modeled by specifying a logarithmic profile for the wind velocity at the inlet [13]. The

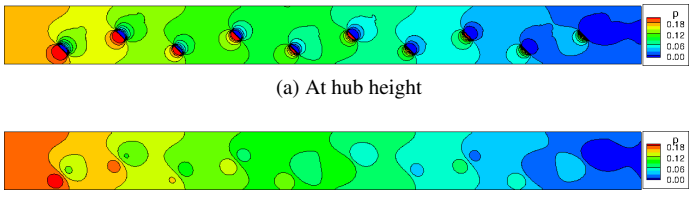

(a) At hub height

(b) On the ground

FIGURE 18: Inviscid simulation: Kinematic pressure contours drawn (a) at hub height and (b) on the ground.

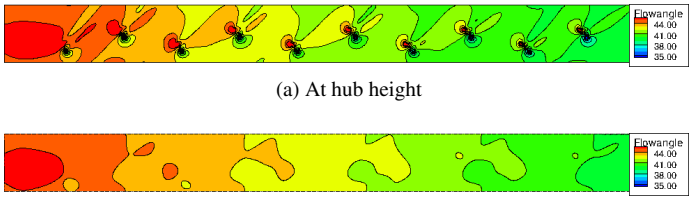

(a) At hub height

(b) On the ground

FIGURE 19: Inviscid simulation: flow angle (w.r.t. x direction) contours drawn (a) at hub height and (b) on the ground.

velocity is determined using

$$u = \frac{u^*}{\kappa} ln\left(\frac{z - z_g}{z_0}\right), \tag{8}$$

where the Karman constant, $\kappa = 0.41$, surface roughness height, $z_0 = 0.0006$ in the non-dimensional units used, and u^* is specified so as to obtain the mean wind velocity at hub height equal to 1. Figure 20 shows the inlet boundary layer velocity profile applied at the inlet boundary.

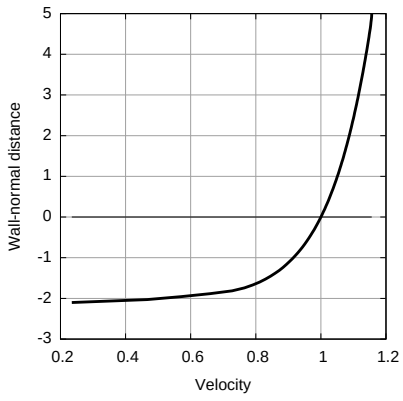

FIGURE 20: Boundary layer velocity profile for viscous simulations.

The ground is modeled using wall functions since resolving to the wall is computationally expensive. Also, the intent here is to show the effect of boundary layer on surface flow convergence and not absolute data comparison. The inflow angle is again set at 45^0. Figures 21 and 22 plot the pressure and flow angle contours at hub height and at a distance slightly above the ground. The spatial variation of pressure between the inviscid and viscous calculations is about the same at both the hub height as well as near the ground (compare Figs. 18 and 21). However, the flow angle variation hear the ground in the viscous case is much larger than for the inviscid case (compare Fig. 19 (b) with Fig. 22 (b)).

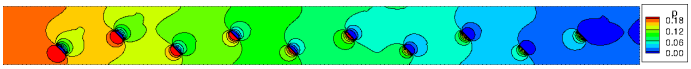

(a) At hub height

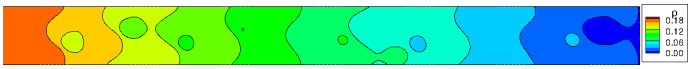

(b) Near the ground

FIGURE 21: Viscous simulation: Kinematic pressure contours drawn (a) at hub height and (b) on the ground.

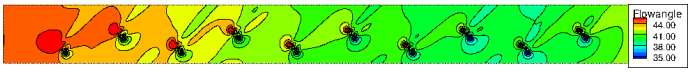

(a) At hub height

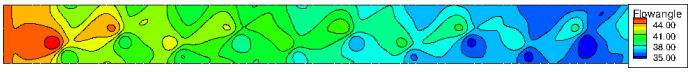

(b) Near the ground

FIGURE 22: Viscous simulation: flow angle (w.r.t. x direction) contours drawn (a) at hub height and (b) on the ground.

Surface flow convergence phenomenon is evident in Fig. 22. While no direct comparison to data in Fig. 16 is attempted here, a quantitative measure of flow deviation is desirable to build confidence in the analyses. Data on the ground plane is averaged along the $y-$direction to study the variation of flow angle with downstream distance, which is plotted in Fig. 23. The flow enters the domain on the left at 45^o angle. The flow angle drops successively behind each turbine due to the pressure differential imposed by the turbines. Flow angle deviation of as much as 9 degrees is observed in these predictions. This is of the same order as the experimental observations (see Fig 16.

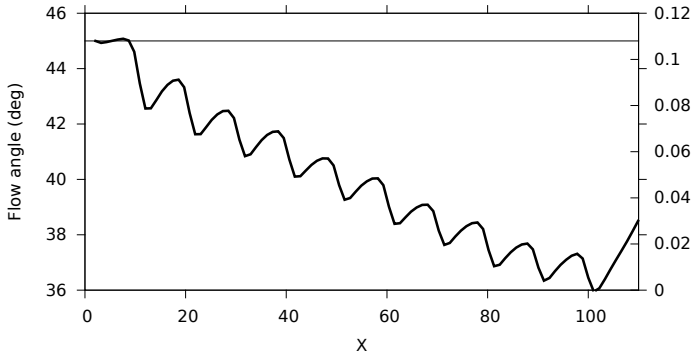

FIGURE 23: Average (over Y direction) flow angle on the ground versus distance along turbine array.

CONCLUSION

A more realistic estimate of the maximum potential C_P of a HAWT is derived using different aerodynamic theories and models. Starting from the 1-D momentum theory, several assumptions are relaxed one by one to quantify the effect on C_P of each physical phenomenon/constraint, i.e., the effect of swirl, number of blades, and viscosity. The efficiency modern HAWTs is found to be only a few percentage points lower than the entitlement.

An actuator disk model is implemented in the OpenFOAM software. SimpleFOAM, that solves steady, RANS equations with the $k-\varepsilon$ turbulence model, is the base solver in which the actuator disk model is implemented. The solver is validated against 1-D momentum theory results for the uniformly loaded rotor. Comparison with experimental data and BEM theory are also performed for two experimental turbines. The agreement with data/theory is found to be good near peak performance and deteriorates as the turbine loading or the overall thrust coefficient is increased far beyond the peak performance.

The actuator disk model is used to study a micro-scale meteorological phenomenon called "flow convergence". Flow coming at an angle to an array of wind turbines has been observed to change its direction towards the turbine row direction. A micro-scale low-pressure inside the turbine array is believed to be the reason for this flow convergence. To substantiate this hypothesis, a hypothetical wind farm, with periodic (in one direction) boundaries, is analyzed using the actuator disk model implementation in OpenFOAM. Simulations are first conducted with inviscid flow approximation (uniform flow at inlet). The pressure drop inside the turbine array is observed however the magnitude of flow convergence is found to be much smaller than measured. A viscous simulation with prescribed logarithmic planetary boundary layer at the inlet of the CFD domain is then conducted which exhibits similar pressure drop as in the inviscid case, however the flow turning near the ground is observed to be much larger (of the order of measured values). The reduced dynamic pressure (because of reduced velocity in the boundary layer) is responsible

for the larger turning near the ground.

ACKNOWLEDGMENT

The authors would like to thank Prof. Eugene Takle and Dr. Daniel Rajewski for providing experimental data on flow convergence and for several technical discussions on modeling efforts.

REFERENCES

[1] Barthelmie, R. J., 2007. "Modeling and measurements of wakes in large wind farms". *Journal of Physics: Conference Series,* ***75***.

[2] Takle, E. S., 2012. Private communication.

[3] Betz, A., 1919. "Schraubenpropeller mit geringstem energieverlust.". PhD thesis, Gottingen Nachrichten.

[4] Goldstein, S., 1929. "On the Vortex Theory of Screw Propellers". *Proceedings of the Royal Society A: Mathematical, Physical and Engineering Sciences,* ***123***(792), Apr., pp. 440–465.

[5] Okulov, V. L., 2004. "On the stability of multiple helical vortices". *Journal of Fluid Mechanics,* ***521***, Dec., pp. 319–342.

[6] Okulov, V. L., and Sørensen, J. N., 2008. "An ideal wind turbine with a finite number of blades". *Doklady Physics,* ***53***(6), July, pp. 337–342.

[7] Okulov, V. L., and Sørensen, J. N., 2008. "Refined Betz limit for rotors with a finite number of blades". *Wind Energy,* ***11***(4), July, pp. 415–426.

[8] Wilson, R. E., Lissaman, P. B. S., and Walker, S. N., 1976. "Aerodynamic performance of wind turbines". *NASA STI/Recon Technical Report N,* ***77***, June, pp. 18598–+.

[9] Mikkelsen, R., 2003. "Actuator disk models applied to wind turbines". PhD thesis, Technical University of Denmark.

[10] J. G. Schepers, A. J. Brand, A. Bruining, J. M. R. Graham, M. M. Hand, D. G. Infield, H. A. Madsen, R. J. H. Paynter, and D. A. Simms, 1997. "Final report of iea annes xiv: Field rotor aerodynamics". *ECN-C–97-027*.

[11] M.M. Hand, D.A. Simms, L.J. Fingersh, D.W. Jager, J.R. Cotrell, S. Schreck, and S.M. Larwood, 2001. "Unsteady Aerodynamics Experiment Phase VI: Wind Tunnel Test Configurations and Available Data Campaigns". *NREL Technical Report, NREL/TP-500-29955*.

[12] I. H. Abbott, and A. E. von Doenhoff, 1959. *Theory of Wing Sections Including a Summary of Airfoil Data*. Dover Publications, Inc.

[13] D. M. Hargreaves, and N. G. Wright, 2007. "On the use of the k-epsilon model in commercial cfd software to model the neutral atmospheric boundary layer". *Journal of Wind Engineering and Industrial Aerodynamics,* ***95***, pp. 355–369.